

Review of thermal infrared polarimetry, part 2: experiment

Nathan Hagen *

Utsunomiya University, Department of Optical Engineering, Utsunomiya, Japan

Abstract. After the discussion on thermal polarization theory from part 1 of this review, we now review practical methods for experimentally measuring infrared polarization properties. Starting with a model for thermal emission from inhomogeneous media, we discuss the complexities of paints and how to determine the ideal thickness of paints used for blackbody simulators. Another commonly used inhomogeneous material is anodized aluminum, and we provide an extensive discussion of its fascinating structure and its optical properties in the thermal infrared. Theoretical analysis and experimental measurements show how the peculiar properties of alumina in the longwave infrared region combine to create a material that has a surprisingly high emissivity, for optically smooth sapphire and highly inhomogeneous anodize-coated aluminum. To illustrate features of thermal polarization theory given in part 1 of this review, we also present a series of infrared polarization images, and demonstrate the use of a convenient reference source for thermal polarization testing. © 2022 Society of Photo-Optical Instrumentation Engineers (SPIE) [DOI: [10.1117/1.OE.61.8.080901](https://doi.org/10.1117/1.OE.61.8.080901)]

Keywords: infrared; polarization; emissivity; blackbody; Kirchhoff's law; paint; anodization; alumina.

Paper 20220229V received Mar. 8, 2022; accepted for publication Aug. 9, 2022; published online Aug. 26, 2022.

1 Introduction

Part 1 of this review focused on the theory needed to understand polarization behavior in the thermal infrared, with a particular emphasis on the physics underlying thermal emission.¹ In this part, we cover thermal polarization measurements, and particularly focus on how we can interpret measurements in situations where we cannot control or accurately quantify many of the variables involved in a measurement. This is a common problem for outdoor measurements, or when measuring surfaces with unknown optical properties. Whereas textbook examples of measurements are often limited to well-controlled situations that are only available in a lab, the discussion that follows aims to show how to interpret measurements of things such as the optical and thermal behavior of a paint layer and its metal substrate, how they interact when exposed to sunlight or night sky, and how their behavior changes depending on the thickness of the paint coating. Moreover, in outdoor environments, we often do not know the background spectrum of the light being reflected from a surface. As a result, such measurements can involve a bit of detective work, combining thinking about the underlying physics with building approximate thermal models for the materials, to make sense of measurements.

The discussion that follows starts with practical techniques to obtain the reflectivity and emissivity. Section 3 then describes how paints behave in the thermal infrared region, and how one can use this information to decide on the ideal coating thickness for a blackbody simulator using high-emissivity paint. The discussion of different types of paints and paint coatings brings together material that is difficult to find in the research literature, yet is helpful for considering measurements of car bodies, building exteriors, and coated objects.

Another common complicated material found in almost every lab is anodized aluminum. Section 4 describes the structure of these coatings, how they are created, and the reason for their surprisingly high emissivity. While the behavior of these anodize coatings is “obvious”

*Address all correspondence to Nathan Hagen, nh@hagenlab.org

in hindsight, we show that they perform optically much the same as a pure unstructured slab made of alumina (amorphous sapphire) glass.

Although the radiance from paints and anodize coatings turns out to have little polarization content, other situations show significant polarization, and so Sec. 5 reviews the special requirements of polarimetric data and how to obtain the Stokes parameters with a rotating wire grid polarizer. We then show an easily constructed reference source for thermal polarimetric imaging—a painted light bulb—and how to make use of it in laboratory measurements. Finally, we present a collection of outdoor polarization images taken in both the midwave infrared (MWIR) and longwave infrared (LWIR), to show quantitatively the magnitude of polarimetric signatures found in the thermal regime.

2 Combined Radiance from Emission and Reflection

In most outdoor environments, thermal contrast is driven primarily by two sources: warming sunlight and cooling sky. After dawn, sunlight begins to warm up surfaces that it touches, at a rate faster than the surrounding air. For objects exposed to sunlight, the surface temperature is driven by the amount of sunlight that it absorbs versus the rate at which the surface transfers heat to its surroundings via conduction, convection, and radiation. For objects that remain in the shade, or which equilibrate to the local air temperature (as plants do using transpiration), thermal contrast remains small.

In the MWIR and LWIR measurement windows (3 to 5 μm and 8 to 12 μm , respectively), thermal photons radiated by surfaces into a cloudless sky have a high chance of escaping into space. Because a cloudless sky also has low thermal emission, this allows sky-facing surfaces to cool down in proportion to the solid angle of clear sky visible to them. Though outer space has an effective temperature of only 3 K, atmospheric transmission in the window regions is not 100% so the night sky never gets as cold as that, but can reach -100°C for wavelengths near 10 μm , at the center of the LWIR window, when viewing through dry air.

Because the night cooling process is dominated by radiative cooling whereas the morning warming process is dominated by sunlight absorption, objects generally warm up in the morning faster than they cool down at night. These two processes drive the development of thermal contrast between objects in the outdoors, and consequently the production of thermal polarization signatures.

Figure 1 shows the radiance reaching a thermal infrared camera, where the at-sensor radiance is a sum of the object surface’s self-emission $L_{\text{obj}} = \epsilon L_{\text{bb}}(T_{\text{obj}})$ and the reflected radiance from the background, ρL_{bkg}

$$L_{\text{meas},m} = \epsilon_{\text{obj},m} L_{\text{bb}}(T_{\text{obj}}) + \rho_{\text{obj},m} L_{\text{bkg},m}, \tag{1}$$

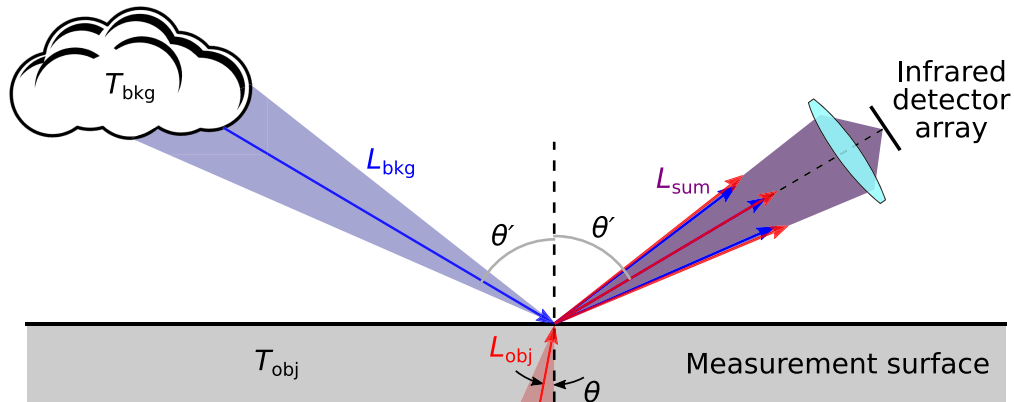


Fig. 1 The measurement geometry, showing the object emission (in red) and background reflection (in blue) components of thermal radiance detected by the camera. The thermal contrast is $\Delta T = T_{\text{obj}} - T_{\text{bkg}}$, and the radiance contrast is $\Delta L = L_{\text{obj}} - L_{\text{bkg}}$.

for polarization $m \in \{s, p\}$. Each of the quantities here also depends on the wavelength λ and the direction of emission/reflection θ' , but explicitly showing these dependencies makes the expressions unwieldy, so we leave them implied.

Light from the background passes through the intervening atmosphere before reaching the object surface, and this generally causes absorption of the object's radiance, as well as path-radiance emission by the air. Using Kirchhoff's law to equate the path emission with path absorption, $\epsilon_{\text{path}} = 1 - \tau_{\text{path}}$, we define L_{bkg} as

$$L_{\text{bkg},m} = \tau_{\text{path}}[\epsilon_{\text{bkg},m}L_{\text{bb}}(T_{\text{bkg}})] + (1 - \tau_{\text{path}})L_{\text{bb}}(T_{\text{path}}). \quad (2)$$

If the atmospheric absorption is small enough to be neglected ($\tau_{\text{path}} = 1$), such as when the optical path is short, then substituting Eq. (2) into Eq. (1) and writing $\rho_{\text{obj},m} = 1 - \epsilon_{\text{obj},m}$ gives

$$L_{\text{meas},m} = \epsilon_{\text{obj},m}L_{\text{bb}}(T_{\text{obj}}) + (1 - \epsilon_{\text{obj},m})L_{\text{bkg},m} = \epsilon_{\text{obj},m}\Delta L + L_{\text{bkg}}(T_{\text{bkg}}), \quad (3)$$

for radiance contrast $\Delta L = L_{\text{bb}}(T_{\text{obj}}) - L_{\text{bkg}}$.

When $\rho L_{\text{bkg}} \gg \epsilon_{\text{obj}}L_{\text{obj}}$, the reflected radiance dominates over surface emission, as when the object is much cooler than the background, or when the object emissivity is much smaller than the reflectivity (e.g., polished metals). When $\epsilon_{\text{obj}}L_{\text{obj}} \gg \rho L_{\text{bkg}}$, surface emission dominates over reflection, as when the object is much hotter than the reflected background. This is a common situation when viewing warm objects that have a high emissivity or when the reflected background is very cold (e.g., a cloudless sky).

One of the consequences of Eq. (3) is that, as Tyo et al.² demonstrated, there will be no polarimetric signature when the surface and the reflected background are in radiometric equilibrium, where $\Delta L = 0$.

2.1 Practical Methods of Measuring Reflectivity and Emissivity

In the thermal infrared, it is very difficult to obtain surfaces that are completely dark. Every measurement of a surface is therefore a composite of the surface's self-glow and the background reflected from the object. As a result, one must exploit reference samples to a much larger extent than is necessary in the visible spectrum. For example, while we may wish to measure the reflectivity ρ_{obj} of a surface, the radiance received by the camera depends on multiple unknowns. However, if the object emissive radiance can be ignored (such as when the measurement object is much colder than the reflected background), then we can use a blackbody as background taken at two different temperatures T_1 and T_2 . When we subtract then subtract the two measurements, we obtain

$$L_{\text{obj},1} - L_{\text{obj},2} = \rho_{\text{obj}}[L_{\text{bb,bkg}}(T_1) - L_{\text{bb,bkg}}(T_2)], \quad (4)$$

in which we obtain the reflectivity as

$$\rho_{\text{obj}} = \frac{L_{\text{obj},1} - L_{\text{obj},2}}{L_{\text{bb,bkg}}(T_1) - L_{\text{bb,bkg}}(T_2)}, \quad (5)$$

where L_{obj} is a radiance measured by the camera, and L_{bb} is the blackbody radiance source. Unfortunately, this by itself is not a practical approach for outdoor measurements.

If we can ignore the reflected signal and work with only the emissive radiance, then another approach is possible. For this, we insert into the scene an opaque reference sample of known temperature T_{ref} and emissivity ϵ_{ref} , and take the ratio of the radiance from the object and the radiance from the reference

$$\frac{L_{\text{obj}}(\lambda)}{L_{\text{ref}}(\lambda)} = \frac{q(\lambda)\epsilon_{\text{obj}}(\lambda)L_{\text{bb}}(\lambda, T_{\text{obj}})}{q(\lambda)\epsilon_{\text{ref}}(\lambda)L_{\text{bb}}(\lambda, T_{\text{ref}})}, \quad (6)$$

where $q(\lambda)$ represents the responsivity of the optics and detector, as well as influence of the measurement geometry. In the outdoors, these can be difficult to estimate accurately, but because $q(\lambda)$ can be arranged to be approximately the same for both “obj” and “ref,” we rewrite this as

$$\epsilon_{\text{obj}}(\lambda) = \frac{L_{\text{obj}}(\lambda) L_{\text{bb}}(\lambda, T_{\text{ref}})}{L_{\text{ref}}(\lambda) L_{\text{bb}}(\lambda, T_{\text{obj}})} \epsilon_{\text{ref}}(\lambda), \quad (7)$$

from which we obtain the emissivity estimate. This too is not yet a practical approach since we have had to ignore the reflected radiance.

For a general situation, in which the reflected and emitted radiances are significant, we need to combine the two above. If we measure the detected radiances from the object and the reference, at two different temperatures T_1 and T_2 , we subtract the two measurements and then take the ratio between the object and reference radiances. For a detected radiance from the object,

$$L_{\text{obj}}(\lambda, T) = q(\lambda) [\epsilon_{\text{obj}}(\lambda) L_{\text{bb}}(\lambda, T) + \rho_{\text{obj}} L_{\text{bkg}}(\lambda)], \quad (8)$$

we use the shorthand $L_{\text{obj},1} = L_{\text{obj}}(\lambda, T_1)$ and $\Delta L_{\text{obj}} = L_{\text{obj},2} - L_{\text{obj},1}$ to write

$$\Delta L_{\text{obj}} = q(\lambda) \epsilon_{\text{obj}}(\lambda) [L_{\text{bb},2} - L_{\text{bb},1}], \quad (9)$$

where the background radiance terms have dropped out. Next, we do the same thing for the reference measurements and then take the ratio

$$\frac{\Delta L_{\text{obj}}}{\Delta L_{\text{ref}}} = \frac{\epsilon_{\text{obj}}(\lambda) [L_{\text{bb}}(\lambda, T_{\text{obj},2}) - L_{\text{bb}}(\lambda, T_{\text{obj},1})]}{\epsilon_{\text{ref}}(\lambda) [L_{\text{bb}}(\lambda, T_{\text{ref},2}) - L_{\text{bb}}(\lambda, T_{\text{ref},1})]}, \quad (10)$$

so the emissivity is obtained as

$$\epsilon_{\text{obj}}(\lambda) = \left(\frac{\Delta L_{\text{obj}}}{\Delta L_{\text{ref}}} \right) \left(\frac{L_{\text{bb,ref},2} - L_{\text{bb,ref},1}}{L_{\text{bb,obj},2} - L_{\text{bb,obj},1}} \right) \epsilon_{\text{ref}}(\lambda). \quad (11)$$

In the lucky circumstance where one can ensure that the temperatures T_1 and T_2 are the same temperatures for both the object and the reference, then this simplifies to

$$\epsilon_{\text{obj}}(\lambda) = \left(\frac{\Delta L_{\text{obj}}}{\Delta L_{\text{ref}}} \right) \epsilon_{\text{ref}}(\lambda). \quad (12)$$

One should also keep in mind that the approach shown here gives the emissivity at the particular angle of view at which the measurements were taken. Any change in the view angle, the surface angle, or the background light distribution will require another set of measurements for ϵ under the new conditions.³ The derivation leading to Eqs. (11) and (12) also assumes a specular reflecting surface. For nonspecular reflecting surfaces and nonuniform backgrounds, a fully four-dimensional representation of the incident and reflected light fields becomes necessary.^{4,5}

3 Paint Coatings

Paint consists of a binder (such as a resin or polymer-based oil) mixed with a diluent (such as water or an organic solvent), a colorant (such as pigment particles or dye), an opacifier (such as TiO_2 particles), and other additives. For example, a varnish is considered as a pigment-free paint and an ink is considered as a paint with minimal binder. Because paints are often formed as a colloidal suspension of soluble and insoluble materials, light passing through a paint coating layer will experience the coating as a material with inhomogeneous optical properties. Though one can model the light propagation at the microscale, using Monte Carlo methods and optical models of the various constituents in the paint, this requires considerable work to set up and implement. A more practical approach is to model the paint as a scattering medium with uniform properties of n , k , and scattering coefficient σ that are in some sense an average over the properties of the material mixture.

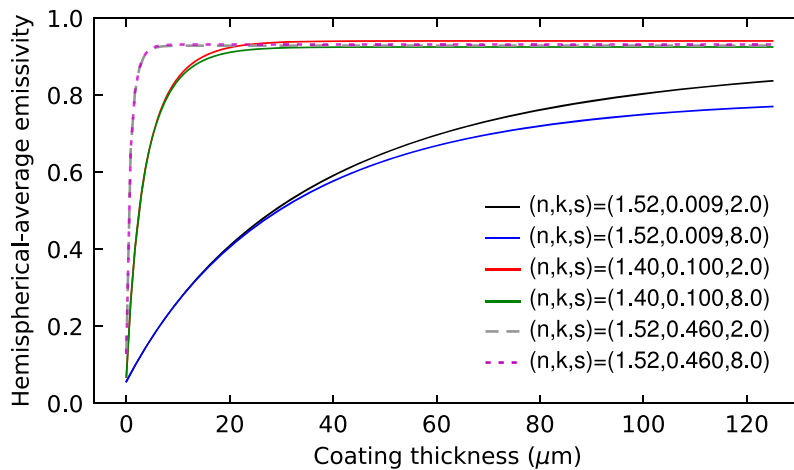


Fig. 2 The hemispherical-average emissivity ϵ as a function of paint coating layer thickness, for various paint optical properties (n, k, s) .

Paints come in a wide variety of materials, so that the exact theoretical models are generally not very useful except as a guide to the overall behavior. Speaking in broad terms, we can say that most paint binders (especially for paints used for visible-light purposes and not specially designed for particular infrared properties) are formed with materials that have a relatively high transmittance in the LWIR region.^{6,7} Most inorganic pigments found in paints have strong, broad absorption bands in the LWIR, with carbonates having absorption bands centered near $7 \mu\text{m}$, silicates near $9 \mu\text{m}$, and oxides between 9 and $30 \mu\text{m}$.⁸ Organic pigments show strong, sharp absorption bands principally between 6 and $11 \mu\text{m}$. Metallic pigments generally exhibit a lower wavelength dependence, and generally reduce the emissivity of a paint.

Painters generally consider a typical paint coating thickness for interior walls of building (using a brush or roller) to be about $50 \mu\text{m}$. Paints applied by spray application tend to have lower concentration of solids and higher concentration of solvents, so that a paint coating applied with a spray can achieve thicknesses as low as $2 \mu\text{m}$.⁹ For industrial coatings such as used on automobile exteriors, multiple paint layers (e.g., primer, base, and enamel) are common, so that the total coating thickness of $>200 \mu\text{m}$ is not unusual. As a result of the high absorbance of dyes and pigments mixed with the paints, these coatings often produce a high emissivity ($\epsilon > 0.9$) at these standard thicknesses.⁶

Using the Kubelka–Munk model of light propagation in scattering media (from section 9 of part 1 in this review), we can estimate the effect that internal scattering has on the reflection and emission properties of a given paint coating in the longwave infrared. Figure 2 shows the estimated emissivity as a function of coating thickness, using equation (59) from part 1 of this review, for a set of paint coating layer properties (n, k, s) , where $s = \sigma\eta$. We can see that in the regime simulated here, of refractive index $1.40 < n < 1.52$, absorption coefficient $0.009 < k < 0.46$, and scattering coefficient $s = 8 \text{ mm}^{-1}$, that the absorption coefficient range plays the largest role in affecting changes in emissivity. With these parameters, we find that the critical thickness of the coating layer is $b_c = 5, 23, \text{ and } 114 \mu\text{m}$ when $k = 0.009, 0.1, \text{ and } 0.46$, respectively.

3.1 Choosing the Ideal Paint Thickness for a Blackbody Simulator

In a laboratory setting, it is common to paint aluminum or copper parts with a high-emissivity matte paint to create a blackbody simulator for the purposes of calibration and creating well-defined thermal sources. Two examples are shown in Fig. 3, of a painted shutter intended for camera calibration, and a painted kitchen pot placed on a heater stove. The paint used here is Krylon 1602 ultraflat black paint. Surprisingly, the painted kitchen pot is actually one of the most versatile and reliable thermal sources that the author has used, having a larger thermal mass and larger area than commercial blackbody sources do, while also allowing a means of quickly changing the temperature by replacing the water inside.

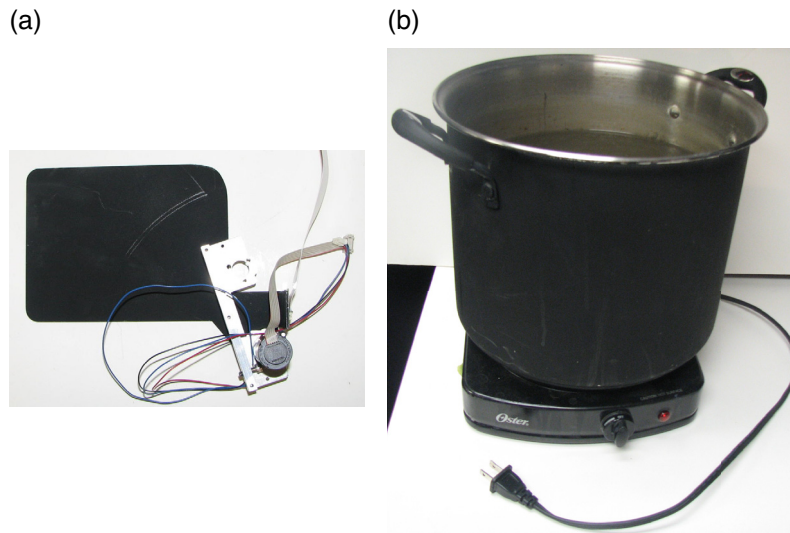


Fig. 3 Two blackbody simulators commonly used in laboratory infrared imaging: (a) a metal shutter and (b) a heated kitchen pot, each coated with a high-emissivity paint.

When constructing these blackbody simulators out of painted metal surfaces, we select metals having high conductivity so that the metal surface is maintained at more-or-less the same temperature as the heat source. (In the case of the kitchen pot, the heat source is the water in the pot.) Next, it is useful to know how thick the paint coating should be. A coating that is too thick will create a thermal insulation barrier against the heat source, so that the coating surface will be significantly cooler than the heat bath, because it is radiating into the cooler ambient air, and is also cooled by air convection currents. A thick paint coating will also make the blackbody simulator susceptible to changes in temperature due to turbulent air currents and changing external heat sources. In contrast, a coating that is too thin will have a reduced emissivity, because the metal substrate will be close enough to the surface to influence the emissivity value. Thus, a coating should be as thick as it needs to be—the critical thickness b_c —but no more.

Unfortunately, the many differences among paint types means that it is very difficult to specify b_c except in broad terms. In Fig. 2, we see three models of paint layers, for which b_c varies from $5\ \mu\text{m}$ —close to the minimum thickness at which a paint layer can be applied—to $225\ \mu\text{m}$, which is a rather thick coating. Sharma et al.¹⁰ recommend an optimal paint coating thickness of 50 to $60\ \mu\text{m}$ for high-emissivity paints. While one can use a paint thickness gauge to achieve the desired thickness, in practice the difference among paints means that it is necessary to measure each paint experimentally to determine b_c . Though this is not difficult, a ready shortcut is available. In the author's experience, the transmittance of the Krylon 1602 black paint in the visible spectrum is actually not far from the transmittance in the LWIR region, so that one can judge the correct thickness by painting a transparent sample such as an acrylic plate and place a bright light source behind the sample. Once the fully dried paint layer is opaque enough that the light source is no longer visible, the paint layer is also close to b_c for LWIR light. Using the same paint techniques to achieve an equivalent thickness on the metal part is a simple matter of practice and care.

One question that arises for painted-metal blackbody simulator sources is how these can be considered blackbodies if the paint layer, being a thermal insulator, produces a thermal gradient between the substrate and the surface. If we compare the paint coating to a blackbody of equivalent *surface* temperature, then the paint will be unfairly biased and we might obtain $\epsilon > 1$ because the warmer inner layers of the paint will be emitting more light than they should be under an isothermal assumption. Of course, when we make the blackbody, we can compensate for this by calibrating the simulator to drive the metal to a slightly lower temperature, but clearly this is an expediency. As long as the correction is small enough, however, the blackbody simulators remain useful sources to have in the lab.

Section 7.2 in part 1 of this review dealt with this issue and simulated the case for paint coatings, concluding that for high-emissivity paints the isothermal requirement can be ignored in the LWIR regime. For low-emissivity paints, however, it is possible to have modest deviations from the expected emissivity limits when comparing emission with a blackbody at the object's surface temperature. In the MWIR regime, however, where the absorption of the paint base becomes small, there is a much higher likelihood of seeing a significant boost to apparent emissivity ($M > 0$) when heating the surface from behind, and when the paint contains few particulate absorbers (such as for a clear coat).

4 Anodized Aluminum Coatings

Aluminum parts used in manufacturing are often anodized rather than painted, because anodize coatings are generally much stronger than paint, and adhere better to the metal, making them less prone to damage from aging and wear. In optomechanics, anodize coatings are almost always given a black coloring to reduce stray light, though matte paint actually does a better job at this than the anodize coatings can. Although anodize coatings may also be more brittle than paint coatings, making them more susceptible to cracking from thermal stress, the hard layer provides good protection against wear and corrosion. However, it is not clear what role the anodizing plays for thermal infrared systems. Thermal infrared optics also use black-anodized aluminum mounts, but it is not clear from the literature whether this is simply a matter of habit among optics manufacturers, or whether the anodizing provides a useful role in reducing unwanted thermal gradients.

Aluminum metal naturally forms a thin layer of amorphous oxide film (alumina) on its surface when exposed to air.¹¹ Although this 2 to 4 nm natural Al_2O_3 coating is quite hard, it is generally too thin to protect the underlying metal against damage. As a result, many manufacturers apply an electrolytic process to increase the oxide layer thickness, creating either a uniform "barrier" oxide layer or a porous anodize layer.

Nonporous "barrier oxides" are grown in electrolytic solutions in which the aluminum oxide is chemically neutral, while porous oxide coatings are grown within an acidic electrolyte bath—typically sulfuric acid in the case of aluminum—in which the alumina is partially dissolved. For a barrier oxide coating, when an electrical current is applied to the aluminum substrate through the electrolyte, the electric field causes the negatively charged oxide ions to move inward to react with aluminum at the metal-oxide interface.¹² This causes a migration of aluminum atoms out from the substrate while also pushing the oxide layer deeper into the substrate. The positively charged aluminum ions pulled out from the substrate are attracted to the interface between the oxide coating and the electrolyte, allowing the oxide layer to thicken. For a barrier (i.e., nonporous) oxide, the final thickness of the oxide layer depends on the applied voltage, producing about 1.1 nm thickness per volt.¹³ A 100 V process thus generates a barrier oxide thickness of 110 nm, which is much thicker than the original natural oxide layer of 2 to 4 nm.

Although the growth of porous oxide films follows a very similar electrochemical process, they can be formed at much lower voltages by placing the metal inside an acidic solution—typically sulfuric acid in the case of aluminum. Because the aluminum oxide is partially soluble in the acid bath, the surface layer partially dissolves and develops pores.^{14,15} As the anodization proceeds, the pores allow the oxides to continue migrating deeper into the metal substrate than is possible with a barrier oxide, so that the process grows a thick porous layer of aluminum oxide directly out of the aluminum substrate. The size of the pores and rate of oxide layer growth are controlled through the acid concentration, applied voltage, temperature, and aluminum alloy type (for example, see Fig. 4). Typical commercial aluminum anodize may have thicknesses ranging from 2 to 25 μm , with typical pore diameters of 30 nm spaced 100 nm apart.^{17,18}

In precision engineering, a common practical rule followed by designers is that during anodization the aluminum oxide grows equal amounts into the surface as out from the surface, as shown in Fig. 5. By this rule, an anodize layer will increase the original part dimensions on each surface by half the oxide layer thickness.¹⁹ Precise measurements, however, have shown that the actual growth is typically closer to 1.4—that is, the anodization expands the part dimensions by 40% of the thickness of the oxide layer (rather than the 50% given by the common rule).¹⁶

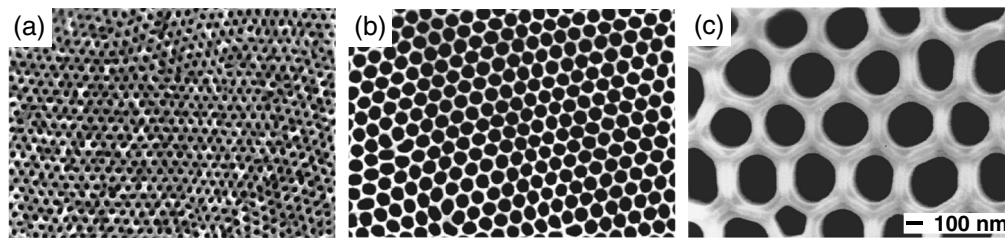


Fig. 4 (a)–(c) Field-emission scanning electron microscopy top view images of anodized aluminum formed at voltages ranging from 20 to 160 V in different acid solutions, showing the change in pore diameter with process conditions. Adapted with permission from Ref. 16.

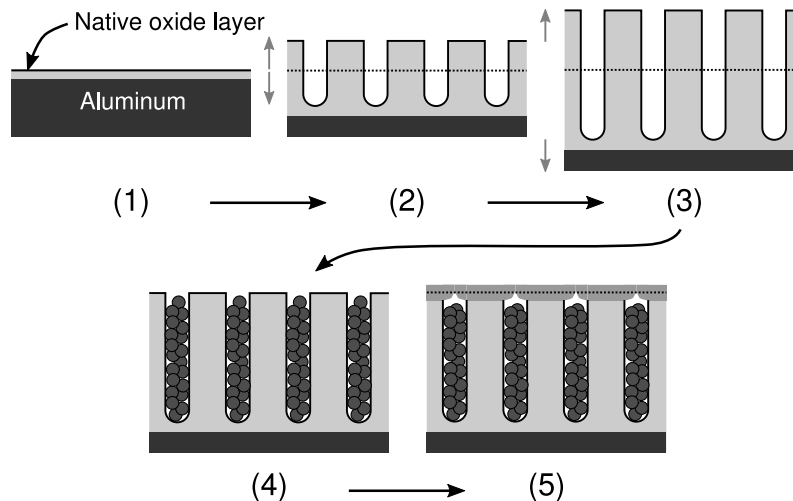


Fig. 5 Cutaway view of the anodize film structure as it develops: (1) the aluminum base metal (dark gray), (2) develops pores of aluminum oxide (light gray) that extend down into the metal and up above the original surface layer. (3) The pores grow over time, after which the metal is removed from the acid bath. (4) The metal is dipped into a bath of dye (with the dye particles shown here as small spheres), which collects inside the pores. (5) The metal is sealed a layer of boehmite (medium gray) at the outer surface that closes the pores.

Li et al.¹⁶ noticed, however, that this growth value can vary considerably with the anodization process used.

At the end of the first anodization step, bare anodized aluminum appears like the unpolished metal, but slightly whitened in color (step 3 in Fig. 5). Because the porous coating is composed of Al_2O_3 , the aluminum now has a very hard surface that is no longer brittle, as it is now much thicker. However, at this point so far it retains most of its natural metallic color. The process of adding color to an anodize can occur simultaneously with the anodization process by adding colorants into the acidic solution. Or, color can be added after completion of the anodize by dipping the anodized metal in one or more warm dye solutions (cobalt acetate and ammonium sulfide are common dyes). This is step 4 in Fig. 5. Whether colored during anodization or after, the coloring process is followed by inserting the metal into either a hot water bath, or into a room-temperature nickel acetate solution, to “seal” the surface (step 5 in Fig. 5).^{20,21} (The nickel acetate $\text{C}_4\text{H}_{14}\text{NiO}_8$ acts as a catalyst for the formation of boehmite.) Most sources describe this sealing process as producing a layer of boehmite ($\gamma\text{-AlO}(\text{OH})$) at the outermost surface of the sample, causing the outermost layer of aluminum oxide to expand. This forces the pores to close, and prevents the enclosed dye from escaping.²² Hu et al.,²⁰ however, show measurements implying that the boehmite also coats the interior walls of the pores. In the end, the resulting seal is effective enough that the colorants enclosed by the anodize layer do not outgas even when exposed to vacuum.¹⁰ Finally, while most of the dyes used for coloring anodized aluminum are susceptible to fading on exposure to strong UV and blue light, a few dyes can retain their color even after extended exposure.

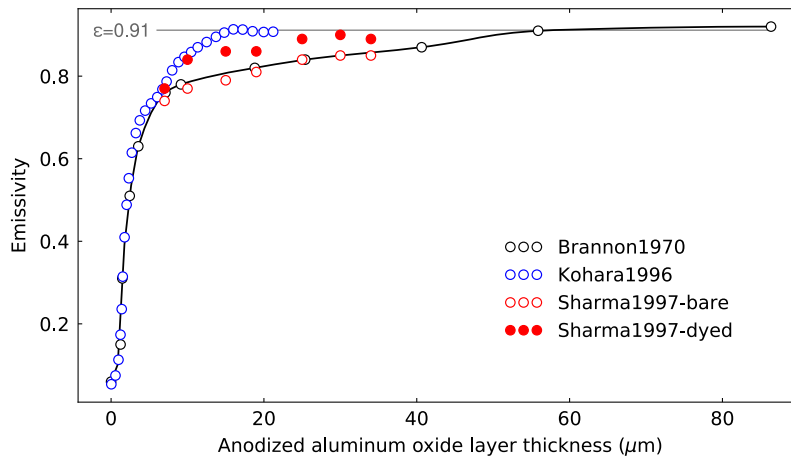


Fig. 6 Measured emissivity of anodized aluminum at normal incidence at $\lambda = 10 \mu\text{m}$, with data taken from Refs. 10, 23, and 24.

Figure 6 shows the normal-angle measurements of anodized aluminum emissivity at $\lambda = 10 \mu\text{m}$, as a function of the anodize layer thickness, obtained from three published sources.^{10,23,24} The Kohara and Sharma measurements in Fig. 6 use a standard anodize coating, while the Brannon measurements use a hard (low-temperature) anodize coating. In each case, from a base polished aluminum emissivity of 0.05, the anodization layer increases ϵ to 0.15 with only $1 \mu\text{m}$ thickness, 0.45 with $2 \mu\text{m}$ thickness. From the collected measurements, we can see that the anodize films reach $\epsilon = 0.91$ at critical thicknesses of $b_c = 15, 25,$ and $50 \mu\text{m}$, respectively, for the Kohara, Sharma, and Brannon data. The Brannon and Kohara data are for an undyed anodize coating, while the Sharma data contain measurements for both undyed and black-dyed anodize. Adding the black dye appears to have increased the emissivity of the coating slightly when the coating is thin, but the dye does not seem to affect the emissivity value for layers above the critical thickness. The larger critical thickness value obtained by Brannon may be a result of the use of a hard anodize process, but may also be due to other differences in the anodize process used.

A final concern is that once the porous anodize oxide layer is sealed, the various sealing methods form a thin layer of boehmite on the outer surface of the coating. Emissivity data on boehmite are quite difficult to find, but Kollie et al.²⁵ presented measurements of boehmite films, giving ϵ from 0.91 to 0.93. Because this value is quite close to the value of the anodize coating itself, it seems that the boehmite layer is unlikely to change the overall emissivity by much.

4.1 Reflectivity Measurements on Anodized Aluminum Parts

To explore how the porous structure of anodize layers and the colorants sealed inside them affect the optical properties in the thermal infrared, we measured the reflectivity of two smooth flat anodized surfaces, from two widely adopted optomechanics manufacturers (Thorlabs BA2/M and OptoSigma CAAN-25LSEE). Choosing smooth samples minimizes the effect of diffuse reflection on the reflectivity measurements. The results of the experimental measurements, taken with a LWIR microbolometer camera (FLIR A35), are shown as dots in Fig. 7, from which we fit polynomial curves. Because it was difficult to control the background source radiance for measurements taken at smaller angles of incidence ($<30^\circ$), the data at these angles is less reliable (as indicated in the figure using unfilled circles for those data points), and these points were given less weight in the fitting. The figure also shows a curve drawn in red representing the theoretical reflectivity curve for Al_2O_3 averaged over the 8 to $12 \mu\text{m}$ wavelength region.

The results of Fig. 7 show that the measured reflectivity of the anodized materials closely corresponds to the theoretical curve for alumina in the LWIR. We can conclude, therefore, that the porous structure and the enclosed dyes play almost no role in the optical behavior of the materials at these wavelengths. It seems likely that the process of sealing the pores has created

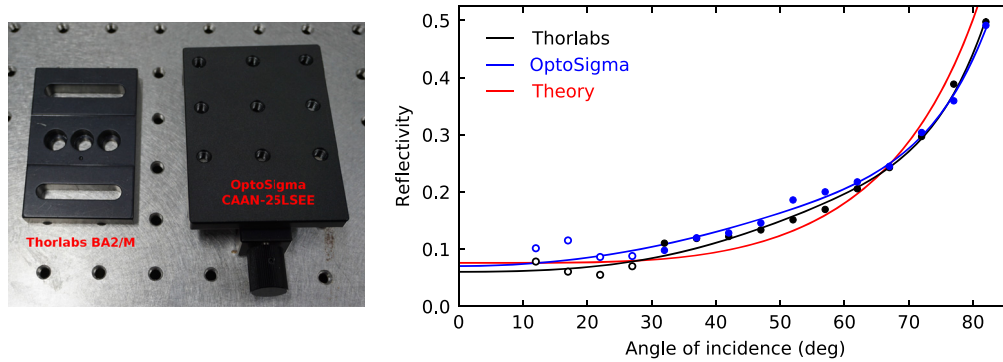


Fig. 7 The experimentally measured reflectivity as a function of angle of incidence. The curves show polynomial fits to the two anodized samples overlaid with the theoretical reflectivity curve for Al_2O_3 averaged across the 8 to 12 μm region.

an external layer of amorphous alumina (or perhaps boehmite) that is sufficiently thick to shield the underlying pores and colorants from affecting the external optical properties. Figure 7 also shows that anodized surfaces have a surprisingly high emissivity at angles near normal incidence—a result that corresponds closely to the data in Fig. 6.

Although the laboratory measurements for Fig. 7 used a rotating wire-grid polarizer in front of the camera to collect the linear polarization state distribution, at none of the measured angles of incidence did the degree of linear polarization (DOLP) exceed 1%, even at grazing angles. Part of the reason for the low DOLP is likely that the reflectivity is already so low that both s and p reflections from the surface will be close in magnitude.

5 Thermal Polarimetry Requires Radiometric Calibration

Thermal imaging data typically come in three types: raw digital counts, temperature units, and radiance units. Temperature units are the most intuitive, but they are unfortunately incompatible with the Stokes vectors, which require the data to be proportional to the at-sensor radiance. While digital counts are proportional to radiance, they are almost always offset by an unknown bias that causes error when calculating quantities related to the degree of polarization (DOP). To illustrate this point, if can measure the light passed by a polarizer at angles 0 deg, 45 deg, 90 deg, and 135 deg, the four intensities (in digital counts and ignoring noise) are given as^{26,27}

$$g_1 = kL_0 + B, \quad (13)$$

$$g_2 = kL_{45} + B, \quad (14)$$

$$g_3 = kL_{90} + B, \quad (15)$$

$$g_4 = kL_{135} + B, \quad (16)$$

for bias value B and unknown constant k . The linear Stokes vector is defined as

$$\begin{pmatrix} s_0 \\ s_1 \\ s_2 \end{pmatrix} = \begin{pmatrix} \frac{1}{2}(L_0 + L_{45} + L_{90} + L_{135}) \\ L_0 - L_{90} \\ L_{45} - L_{135} \end{pmatrix}, \quad (17)$$

so that we can try to take our four measurements g_i with the polarizer to estimate the Stokes vector as

$$\begin{pmatrix} \frac{1}{2}(g_1 + g_2 + g_3 + g_4) \\ g_1 - g_3 \\ g_2 - g_4 \end{pmatrix} = \begin{pmatrix} ks_0 + 2B \\ ks_1 \\ ks_2 \end{pmatrix}. \quad (18)$$

Whereas the bias B drops out of the estimates for s_1 and s_2 , so that these two are estimated accurately despite the bias, the error remains in s_0 . Because the DOLP is calculated from the Stokes vector elements as

$$\text{DOLP} = \frac{\sqrt{s_1^2 + s_2^2}}{s_0}, \quad (19)$$

dividing by s_0 propagates this error into the DOLP result. If B is uncorrected and positive, the estimated DOLP will be too small; if B is negative, then the estimated DOLP will be too large. The same issue occurs when calculating the normalized Stokes parameters $\tilde{s}_1 = s_1/s_0$ and $\tilde{s}_2 = s_2/s_0$. As a result, it is necessary to correct for the bias when working with data in raw digital counts. The bias-corrected digital counts are equivalent to relative radiance units.

The Stokes parameters themselves can be given in absolute radiance units L or relative radiance units kL (with unknown k). When calculating the normalized Stokes parameters or the DOLP, however, the unknown factor drops out of the equations so that the two become identical.

Equation (3) holds for both p - and s -polarizations. If we detect the two polarization states independently, then we write the polarization contrast C as

$$C = \frac{L_p - L_s}{L_p + L_s}, \quad (20)$$

where DOLP is related to the contrast as $\text{DOLP} = |C|$. Another polarimetric parameter that we will have use of below is the angle of linear polarization (AOLP), which is defined as

$$\text{AOLP} = \frac{1}{2} \arctan\left(\frac{s_2}{s_1}\right). \quad (21)$$

It is widely known that smooth surfaces produce polarized reflection and emission, so that man-made objects tend to produce more highly polarized light than natural objects do. And this is especially true in the thermal infrared, because the ratio between the surface roughness and the wavelength is reduced by a factor of 20 in going from visible ($\sim 0.5 \mu\text{m}$) to LWIR ($\sim 10 \mu\text{m}$) wavelengths. Surfaces that are optically rough in the visible can often become optically smooth in the LWIR. Even rough road surfaces, such as asphalt and concrete, show significant polarized reflection properties at $10 \mu\text{m}$ wavelengths.²⁸ Nevertheless, researchers used to visible-light polarimetry often experience surprise upon first encountering the extremely low DOP one typically encounters in the thermal infrared. This low DOP is a direct consequence of the complementarity of the emissivity and reflectivity, which tend to cancel one another, and of the fact that the temperatures we usually encounter are a small ΔT (e.g., $\pm 10 \text{ K}$) on top of a large baseline temperature T_0 (e.g., 300 K). From a radiance standpoint, the temperature contrast we experience in common thermal scenes is small (often $\sim 10\%$) in comparison with the contrast between light and dark in the visible spectrum that we often experience with our eyes (often a factor of 10 or more).

Figure 8 shows an example of reflection of an unpolarized cold object ($T_{\text{bkg}} = 20^\circ\text{C}$) from a warm surface of silica glass ($T_{\text{obj}} = 40^\circ\text{C}$), at angles of incidence $\theta = 0 \text{ deg}$, 30 deg , 45 deg , and 60 deg . At $\theta = 0 \text{ deg}$, the p - and s -polarization spectra coincide, but separate as the incidence angle increases. Thus we see that the polarization contrast for the sum L_{meas} of reflected and emitted light is increasing with angle. We can also see that because the p - and s -polarization reflectivities are equal for silica glass at about $8.5 \mu\text{m}$, the polarization contrast at this wavelength is zero for all angles. Thus, as implied by Eq. (3), we see that when the radiance contrast between the surface and the background reflected from it is small, the polarization-dependence in ϵ_{obj} has little effect.

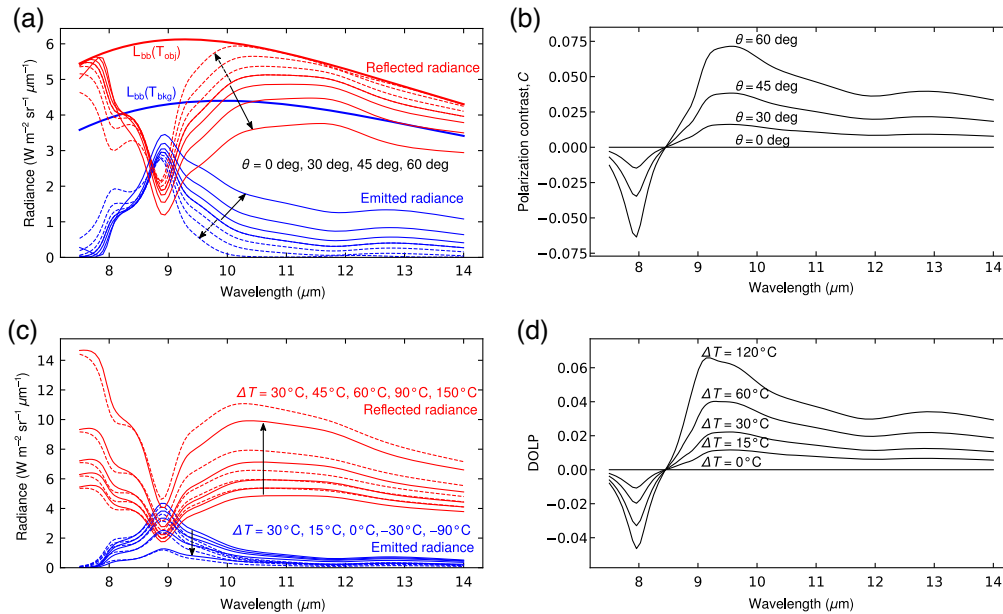


Fig. 8 The p - and s -polarized radiance spectra (solid and dashed curves, respectively) of a SiO_2 glass surface: (a) for $T_{\text{obj}} = 40^\circ\text{C}$, reflecting a background blackbody at $T_{\text{bkg}} = 20^\circ\text{C}$, for angles of incidence $\theta = 0$ deg, 30 deg, 45 deg, and 60 deg. Each arrow indicates the direction of increasing angle; (b) the polarization contrast $C(\theta)$ for the data shown in panel (a). (c) The radiance spectra for an angle of incidence of $\theta = 30$ deg, for increasing amounts of thermal contrast $\Delta T = 0^\circ\text{C}$, 15°C , 30°C , 60°C , and 120°C ; (d) the polarization contrast $C(\Delta T)$ for the data shown in panel (c).

6 Painted Tungsten Bulb for a Thermal Polarimetry Reference Source

To validate polarization measurements, it is important to have a trustworthy reference source against which one can check the results. One useful idea put forward by Bowers et al.²⁹ is to use a large sphere heated to a high temperature and coated with a high-emissivity material. For this, they used a 45-cm diameter hollow brass sphere, painted with high-emissivity paint ($\tilde{n} = 1.6 + i0.1$), with a heater placed inside the sphere. Although this reference source should not be difficult to make, it is also not something that one can get off-the-shelf. Similarly, Kudenov et al.³⁰ used a 125-mm diameter sphere of obsidian glass. In this case, the sphere was heated by immersion in warm water before being dried and placed for imaging. While this too is a useful reference object, it is not as easily obtained, and not as convenient as we might like.

A similar style of reference source that is readily obtained is a spherical tungsten light bulb. This kind of bulb is a reasonable approximation to a true sphere, inherently contains a heater element, and achieves impressively high temperatures. An example set of images of this kind of bulb is shown in Fig. 9. From the images, one can immediately see that the glass of the bulb is actually diathermous, so that the internal tungsten element saturates the image. While glass is an absorbing material in the MWIR range, the bulb glass is evidently too thin to absorb enough of the infrared light. As a result, it is necessary to paint the bulb to increase its opacity. Not only does this increase the surface emissivity, but it also helps increase the surface temperature by absorbing the bulk of the light emitted by the bulb.

Figure 10 shows the same bulb after applying a black paint. As mentioned in Sec. 3.1, one should apply paint as thinly as possible, but sufficiently thick to fully obscure the substrate. In Fig. 10, we can see that the filament is no longer saturating the MWIR camera, but it is nevertheless still visible as the brightest feature in the data. Thus, the paint layer is a little bit too thin. The visible camera image also shows that the black paint does not entirely obscure the visible-spectrum light underneath, and so the visible image can be used as a rough guide to the behavior in the thermal infrared as well. Note that the integration time used in Fig. 9 is longer than that used in Fig. 10 due to the hotter bulb surface of the latter.

One concern with applying black paint to a bulb is that the paint should be designed for high temperature use. Ordinary paints will likely start to burn after extended use of more than couple

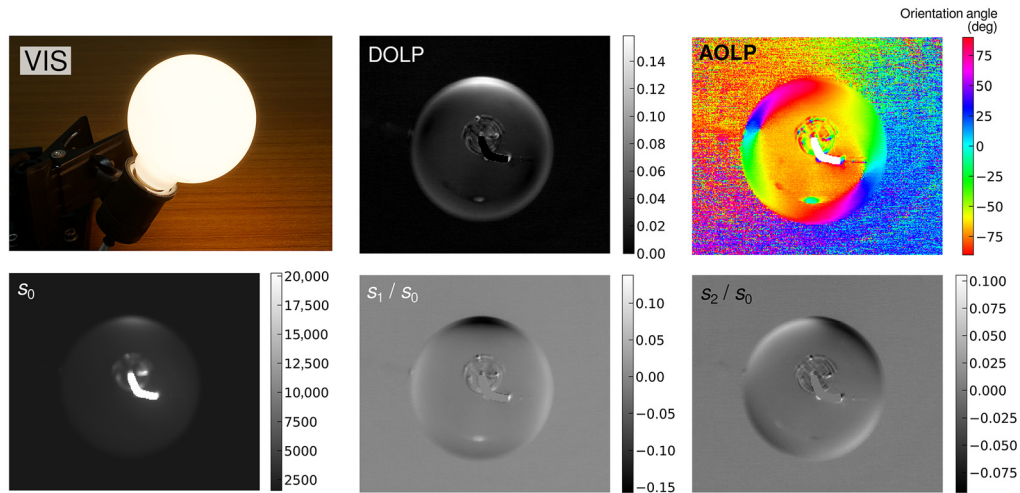


Fig. 9 MWIR polarization images of an unpainted tungsten lamp with a spherical bulb. The s_0 image is given in units of digital counts, with bias term removed.

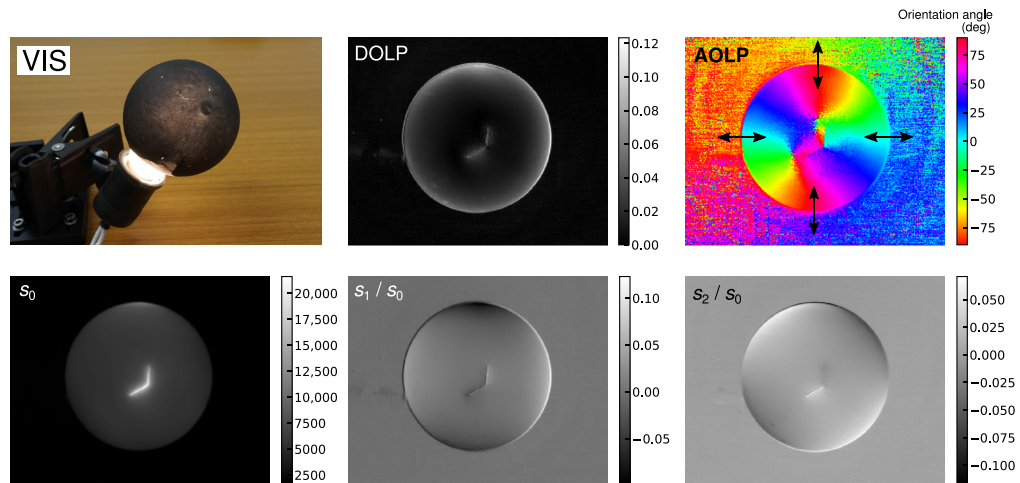


Fig. 10 MWIR polarization images of a tungsten lamp with a spherical bulb painted with black heat-resistant paint. The s_0 image is given in units of digital counts, with bias term removed. The black arrows in the AOLP figure indicate the AOLP direction at the edge of the sphere.

of minutes. In addition, anyone who might want to give this a try should exercise caution. The bulb glass is not designed for temperatures this high, and is also not designed for the additional mechanical constriction forced on it by the paint coating. As a result, there is some risk that the bulb may shatter. This has not yet occurred in any of my own experiments, but it remains a safety concern.

Taking advantage of the painted spherical bulb as a reference source, we use the data of Fig. 10 to check our polarization results. We expect emission to be predominantly p -polarized, so that the angle of polarization will follow the angle of the radius extended from the center of the sphere, with respect to horizontal. Tracing the data along a circle just inside the edge of the reference sphere image gives the AOLP data shown in Fig. 11. Most of the measured AOLP data fall within 5 deg of the ideal polarization angle. The relatively low DOLP of 0.05 is partly due to the roughness of the matte paint surface. (Most high-temperature paints are matte type.) Although we expect the pattern of polarization emission from the sphere to give constant AOLP along radii extending from the center, we can see that the center of the AOLP image shows deviations from this pattern. It seems likely that polarization emission from the filament is

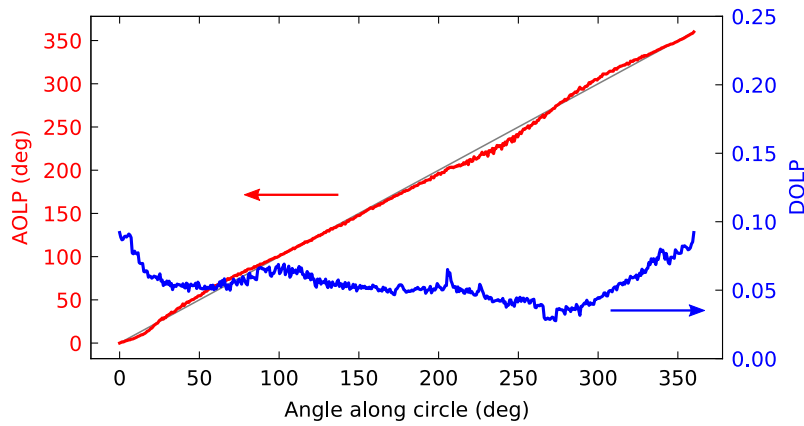


Fig. 11 The AOLP (red curve) and DOLP (blue curve) traced along the circle at the edge of the reference sphere shown in Fig. 10. The slanted gray line shows the ideal polarization angle.

mixing with the bulb surface emission to produce the observed pattern, because the DOLP image clearly shows that the filament is blurred on transmission through the bulb glass and paint.

Finally, in Fig. 12, we show the image of the spherical reference source reflected from a basin of chilled water ($\sim 5^{\circ}\text{C}$). The experiment layout viewed from the side shows that the reflection angle for this setup is roughly 69 deg—somewhat beyond the pseudo-Brewster angle of 53 deg. This is different from the previously stated pseudo-Brewster angle of 50.6 deg because figure 4 in part 1 of this review gives the reflectivity at $10\ \mu\text{m}$, while the camera used here measures in the MWIR ($3\ \text{to}\ 5\ \mu\text{m}$). This angle is still sufficient to generate a strong polarization signature.

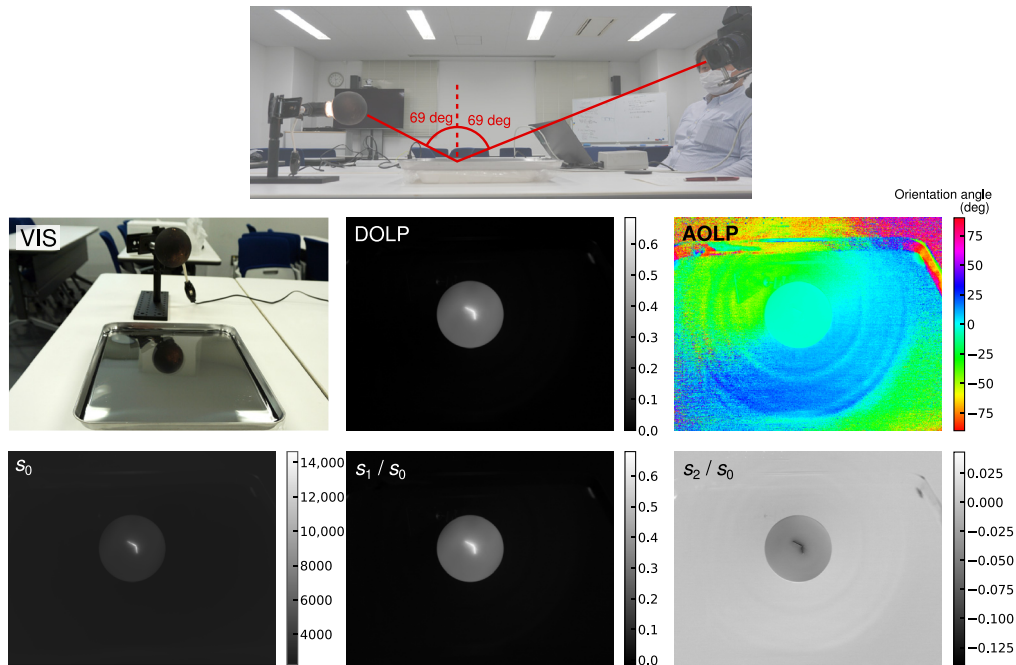


Fig. 12 (Top) The experiment layout, viewed from the side, for measuring the polarization image of the spherical bulb reference source reflected from a basin of chilled water. To the right one can see the wiregrid polarizer and camera lens. (Bottom rows) MWIR polarization images of the black-painted bulb of Fig. 10 seen in reflection from 5°C water, near the pseudo-Brewster angle. Because the water reflection induces a large polarization for objects with such a large thermal contrast, the radial polarization signature seen in Fig. 10 is no longer apparent. The s_0 image is given in units of digital counts, with bias term removed. The concentric circular pattern apparent in the AOLP image is residual calibration error, due to the reflection off the rotating polarizer in front of the camera.

In this case, the rotating AOLP around the edge of the sphere is no longer apparent. Instead, we see only the dominating uniform linear polarization signature due to the water surface reflection. Due to the strong thermal contrast between the reference source and the water, the DOLP achieves a value of about 0.26 over most of the bulb image. Outside of the bulb image, the DOLP generally stays below 0.01 due to the small thermal contrast between the water surface and the reflected room walls.

In the images of Fig. 12, we can also see the image of the tungsten filament inside the bulb reflected from the water. Due to the very large thermal contrast between the filament and the water, we find that the DOLP reaches up to 0.68 for those pixels covering the filament. The pattern of concentric circles surrounding the image of the bulb is due to the linear polarizer. Although the camera's calibration attempted to compensate for the polarizer's effect, the compensation was incomplete, leaving this residual pattern.

7 Collection of Infrared Stokes Vector Imagery of Outdoor Scenes

To demonstrate thermal polarization behavior in the outdoors, Fig. 13 shows a suburban scene of a row of houses illuminated by direct sunlight against a background of blue sky. This data was captured with a FLIR A35 LWIR microbolometer thermal camera, with an image size of 320×256 pixels, $25 \mu\text{m}$ pixel size, 12 bit analog to digital converter (ADC), 50 mK noise-equivalent temperature difference (NETD), and an $f/1.25$ lens. The polarization data were obtained by rotating a wiregrid polarizer, made of aluminum wires deposited on a Germanium substrate, and rotated to azimuth angles of 0 deg, 45 deg, 90 deg, and 135 deg. The s_1 and s_2 images were obtained as in Eq. (17), then divided by s_0 for normalization. Although the s_0 image was calibrated to units proportional to radiance for the purposes of obtaining the Stokes parameters, for purposes of display, the data in Fig. 13 were converted back to radiometric temperature for clarity of discussion, and also to provide an example of the radiometric temperature of the sky.

The solar panel roofing in Fig. 13 is warmed by sunlight, while reflecting a cold background (blue sky). This setup roughly corresponds to the values used in Fig. 8. Because the sky in these images is seen close to the horizon, it is not as cold as when viewed at zenith angle. If we estimate the slant angle of the roof with respect to the line of sight as roughly 30 deg, and that the solar panels are covered with silica glass, then this situation would correspond to the data shown in

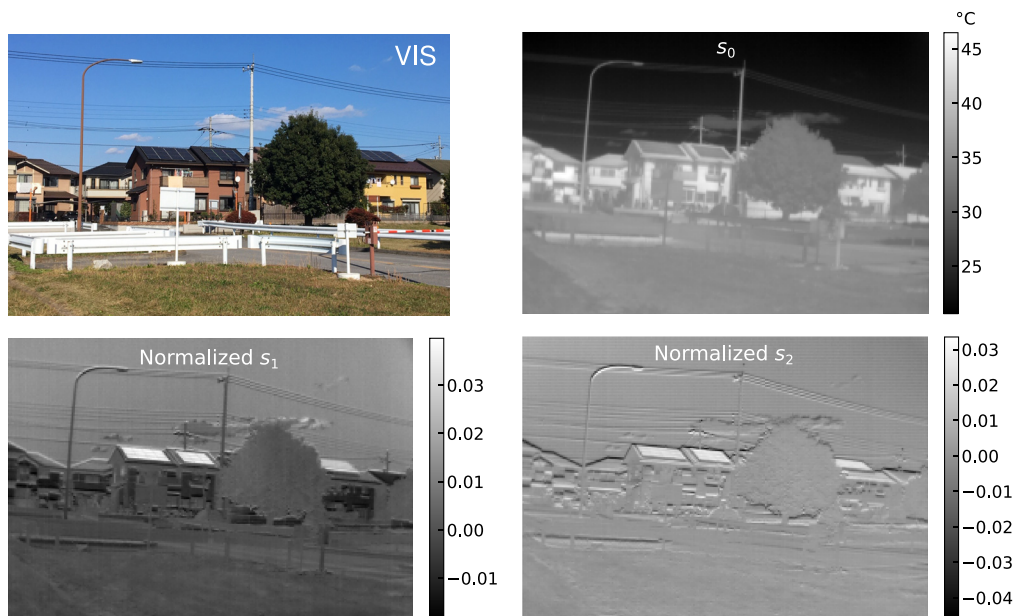


Fig. 13 LWIR polarization images of a row of houses with solar panel roofing. The s_0 radiance image has been converted to temperature units. Due to residual registration errors, object edges in the image contain spurious polarization signatures.

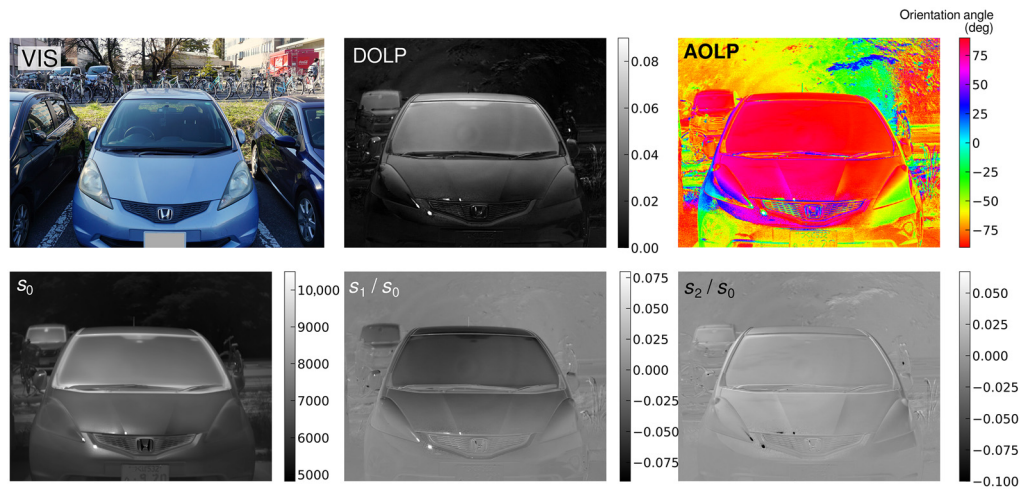


Fig. 14 MWIR polarization images for a car, where the reflected background is primarily blue sky. (The visible and MWIR images were taken at different times.) The faint concentric circles visible in the polarization images are residual calibration errors, due to the reflection off the rotating polarizer in front of the camera.

Fig. 8(d), with the polarization signature averaged across the LWIR band (8 to 12 μm). Solar panels are generally covered with tempered glass, which may have a different reflectance spectrum from pure silica glass, and may or may not be antireflection coated. However, if the solar panel glass is equivalent to silica, we can infer that the thermal contrast between the glass and the reflected background (blue sky) was likely $>40^\circ\text{C}$.

Although the grass and trees in Fig. 13 reflect sky polarization just as the roof panels do, their temperature is lower, due to their transpiration, and their surfaces are also less smooth. In addition, the small size of each leaf means that each pixel in the image contains a range of leaf angles, so that the measured polarization is a sum over a semirandom set of orientation angles. The result is a negligible polarization signature.

The next example (Fig. 14) shows the polarization image of a car, captured with a FLIR x6900sc MWIR InSb thermal camera, with an image size of 640×512 pixels, 25 μm pixel size, 14 bit ADC, 20 mK NETD, and an $f/2.5$ lens. In Fig. 14, the reflected background is once again blue sky, providing a strong thermal contrast for the car body warmed in the sun. Because the reflected background itself is unpolarized, one can use the AOLP defined in Eq. (21) to infer the orientation angle of the surface with respect to the line of sight.

Even under the favorable circumstances of Fig. 14, we can see that the DOP never surpasses 0.1. Although the car windshield, warmed up in the sunlight, is much warmer than the sky background, the radiance contrast is smaller than one might expect because of the 300 K offset to all natural temperatures we experience around us. Though something like 40°C may seem a large thermal contrast, the polarization signature is based to a radiance contrast which would be from, say, a 300 K object and a 340 K object. In terms of temperatures, this is only a 13% difference. For radiances, the ratio will be somewhat larger than this due to the nonlinear relationship.

Note that the faint pattern of concentric rings visible in the polarization images of Fig. 14 appears to be caused by ghost reflections from different surfaces of the camera lens and from the inside surface of the wiregrid polarizer.

8 Conclusion

Although an earlier review of imaging polarimetry suggested that typical polarimetric signatures in the MWIR and LWIR can be as high as 20% to 25%,³¹ my own experience is that typical natural signatures (i.e., outside the lab) generally do not extend beyond 10% except in unusual circumstances.³² The low DOP for most phenomena in the thermal infrared is likely why the field has so far not seen widespread use. Though the polarization signature is useful for applications,

the low DOP means that measurements suffer from a low signal-to-noise ratio except in those circumstances where one can ensure a large thermal contrast between the object under test and the background being reflected from the object. Such circumstances where thermal polarimetry could benefit measurements may be the detection of objects in deep shade or at night, and the measurement of surface orientations from the resulting polarization. In the open ocean, this could potentially include the measurement of wave surfaces at night, if the skies remain clear enough to provide sufficient thermal contrast with the water surface.

As Shaw³³ indicated with respect to thermal polarization measurements containing water reflection, the partial cancellation of reflection and emission polarization is generally more severe in the MWIR than the LWIR, making it more difficult to do emission polarization work in the midwave. In contrast, the MWIR has the advantage that it can work with reflected sunlight, providing with an extremely strong light source for use in reflection polarization that is only available to LWIR measurement through the sunlight's heating of the imaged surface.

In the discussion already noted, we found that blackbody simulators using high-emissivity paints can maintain optimal performance using paint coatings on the order of 20 μm thick. This can be difficult to measure, but one can apply the same painting procedure to a sample that is transparent in the visible spectrum and increase the paint coating until a bright visible light source no longer transmits through the coating. This is a simple rule that can be applied in any laboratory.

We also found that, after anodization, an aluminum surface achieves a surprisingly high emissivity of $\epsilon \approx 0.91$. This is useful in infrared optomechanics, as it helps to homogenize thermal gradients within systems, and gives one reason why the use of anodized aluminum parts is ubiquitous in the field. The discussion also showed that anodize coatings demonstrate a surprisingly complex inhomogeneous structure. Though this makes it difficult to create an accurate optical model of the surface, the fine structure does not seem to have much effect on the optical properties of the material in the thermal infrared. That is, one can treat a dyed anodize coating simply as a slab of amorphous alumina.

The laboratory and outdoor polarization measurements that we presented in Secs. 6 and 7 use only linear polarization states. Though it is possible to generate circular polarization states in the thermal infrared, theoretical considerations tell us that we can expect the degree of circular polarization to be quite small in almost all natural circumstances. However, though circularly polarized emission has not been demonstrated for natural surfaces, it has been shown to exist for nonreciprocal media³⁴ and structured chiral media.^{35,36} For those readers interested in exploring circular states in the thermal regime, there are zero- and low-order quarter-wave plates and half-wave plates that are commercially available for MWIR and LWIR ranges. Most waveplates operating in the MWIR use MgF_2 , while LWIR waveplates are generally made of cadmium thiogallate (CdGa_2S_4), cadmium sulfide (CdS), or cadmium selenide (CdSe). There are even achromatic waveplates made of CdS and CdSe waveplate doublets.

Finally, we can also add that many of the nonthermal phenomena exhibited in infrared emission polarization apply directly to fluorescence emission phenomena as well. As a result, polarization measurement can be used for the separation of fluorescent emission from reflection.^{37,38}

Acknowledgments

The author is grateful to Photron Inc. for allowing use of their FLIR x6900sc InSb camera in the MWIR polarimetry experiments. The author would also like to thank Shuhei Shibata for help conducting the FLIR A35 LWIR polarimetry experiments. A portion of this research was funded by a grant from Denso Corp., and by JSPS KAKENHI (Grant No. JP 20K04516).

References

1. N. Hagen et al., "Review of thermal infrared polarimetry, I: theory," *Opt. Eng.* **61**, 070902 (2022).
2. J. S. Tyo et al., "The effects of thermal equilibrium and contrast in LWIR polarimetric images," *Opt. Express* **15**, 15161–15167 (2007).

3. B. Bartlett et al., "Spectro-polarimetric BRDF determination of objects using in-scene calibration materials for polarimetric imagers," *Proc. SPIE* **7461**, 74610T (2009).
4. W. C. Snyder and Z. Wan, "BRDF models to predict spectral reflectance and emissivity in the thermal infrared," *IEEE Trans. Geosci. Remote Sens.* **36**, 214–225 (1998).
5. I. G. E. Renhorn, T. Hallberg, and G. D. Boreman, "Efficient polarimetric BRDF model," *Opt. Express* **23**, 31253–31273 (2015).
6. J. R. Aronson, "Modeling the infrared reflectance and emittance of paints and coatings," U.S. Army Research Office, 17451.1-0 (1982).
7. B. P. Sandford, "IR reflectance of aircraft paints," Phillips Laboratory, USAF, PL-TR-94-2313 (1985).
8. L. V. Wake and R. F. Brady, "Formulating infrared coatings for defence applications," DSTO Materials Research Laboratory, MRL-RR-1-93 (1993).
9. W. D. McKelvey, P. B. Zimmer, and R. J. H. Lin, "Solar-selective paint coating development," U. S. Department of Energy, DOE/CS/34287-T1 (1979).
10. A. K. Sharma et al., "Anodizing and inorganic black coloring of aluminum alloys for space applications," *Metal Finish.* **95**(12), 14–18 (1997).
11. N. F. Mott, "Oxidation of metals and the formation of protective films," *Nature* **145**, 996–1000 (1940).
12. J. E. Houser and K. R. Hebert, "The role of viscous flow of oxide in the growth of self-ordered porous anodic alumina films," *Nat. Mater.* **8**, 415–420 (2009).
13. R. S. Alwitt, "Anodizing," in *Electrochemistry Encyclopedia*, Electrochemical Society (2002).
14. J. P. O'Sullivan and G. C. Wood, "The morphology and mechanism of formation of porous anodic films on aluminum," *Proc. R. Soc. Lond. A* **317**, 511–543 (1970).
15. C. A. Grubbs, "Anodizing of aluminum," *Metal Finish.* **97**(12), 476–487 (1997).
16. A. P. Li et al., "Hexagonal pore arrays with a 50–420 nm interpore distance formed by self-organization in anodic alumina," *J. App. Phys.* **84**, 6023–6026 (1998).
17. F. Keller, M. S. Hunter, and D. L. Robinson, "Structural features of oxide coatings on aluminum," *J. Electrochem. Soc.* **100**, 411–419 (1953).
18. P. Wade and C. Preedy, "Fujihokka: a high-emissivity approach to aluminum anodizing," *Metal Finish.* **101**(12), 8–13 (2003).
19. S. Liu et al., "Fast anodization fabrication of AAO and barrier perforation process on ITO glass," *Nanoscale Res. Lett.* **9**, 159–166 (2014).
20. N. Hu et al., "Effect of sealing on the morphology of anodized aluminum oxide," *Corrosion Sci.* **97**, 17–24 (2015).
21. S. U. Ofoegbu, F. A. Fernandes, and A. B. Pereira, "The sealing step in aluminum anodizing: a focus on sustainable strategies for enhancing both energy efficiency and corrosion resistance," *Coatings* **10**, 226–280 (2020).
22. C. J. Donahue and J. A. Exline, "Anodizing and coloring aluminum alloys," *J. Chem. Educ.* **91**, 711–715 (2014).
23. R. R. Brannon, Jr. and R. J. Goldstein, "Emittance of oxide layers on a metal substrate," *J. Heat Transfer* **92**, 257–263 (1970).
24. S. Kohara and Y. Niimi, "Infrared radiation properties of anodized aluminum," *Mater. Sci. Forum* **217**, 1623–1628 (1996).
25. T. G. Kollie, T. D. Radcliff, and F. J. Weaver, "Emittance of boehmite and alumina films on 6061 aluminum alloy between 295 and 773K," *J. Heat Transfer* **113**, 185–189 (1991).
26. E. F. Zalewski, "Radiometry and photometry," in *Handbook of Optics*, M. Bass, Ed., Vol. **2**, 2nd ed., Chap. 24, McGraw-Hill (1995).
27. J. R. Schott et al., "Thermal infrared radiometric calibration of the entire Landsat 4, 5, and 7 archive (1982–2010)," *Remote Sens. Environ.* **122**, 41–49 (2012).
28. U. P. Oppenheim and Y. Feiner, "Polarization of the reflectivity of paints and other rough surfaces in the infrared," *Appl. Opt.* **34**, 1664–1671 (1995).
29. D. L. Bowers et al., "Unpolarized calibration and nonuniformity correction for long-wave infrared microgrid imaging polarimeters," *Opt. Eng.* **47**, 046403 (2008).
30. M. W. Kudenov, J. L. Pezzaniti, and G. R. Gerhart, "Microbolometer-infrared imaging Stokes polarimeter," *Opt. Eng.* **48**(6), 063201 (2009).

31. J. S. Tyo et al., "Review of passive imaging polarimetry for remote sensing applications," *Appl. Opt.* **45**(22), 5453–5469 (2006).
32. S. H. Sposato et al., "Two long-wave infrared spectral polarimeters for use in understanding polarization phenomenology," *Opt. Eng.* **41**, 1055–1064 (2002).
33. J. A. Shaw, "Degree of linear polarization in spectral radiances from water-viewing infrared radiometers," *Appl. Opt.* **38**, 3157–3165 (1999).
34. Y. Wang et al., "Broadband circularly polarized thermal radiation from magnetic Weyl semimetals," *Opt. Mater. Exp.* **11**, 3880–3895 (2021).
35. J. Ginn et al., "Polarized infrared emission using frequency selective surfaces," *Opt. Express* **18**, 4557–4563 (2010).
36. C. Khandekar and Z. Jacob, "Circularly polarized thermal radiation from nonequilibrium coupled antennas," *Phys. Rev. App.* **12**, 14053–14064 (2019).
37. O. Sandus, "A review of emission polarization," *Appl. Opt.* **4**, 1634–1642 (1965).
38. S. Ahmed et al., "Separation of fluorescence and elastic scattering from algae in seawater using polarization discrimination," *Opt. Commun.* **235**, 23–30 (2004).

Nathan Hagen: Biography is not available.